

CONSTRAINING THE HIGH DENSITY NUCLEAR SYMMETRY ENERGY WITH PIONS

By

Justin Estee

A DISSERTATION

Submitted
to Michigan State University
in partial fulfillment of the requirements
for the degree of

Physics – Doctor of Philosophy

2019

ABSTRACT

CONSTRAINING THE HIGH DENSITY NUCLEAR SYMMETRY ENERGY WITH PIONS

By

Justin Estee

Copyright by
JUSTIN ESTEE
2019

ACKNOWLEDGEMENTS

Your acknowledgements here.

TABLE OF CONTENTS

LIST OF TABLES	vi
LIST OF FIGURES	vii
CHAPTER 1 EXPERIMENT	1
1.1 Operational Principles of Time Projection Chambers	1
1.2 S π RIT TPC Overview	2
1.2.1 Field Cage	4
1.2.2 Voltage Step Down	8
1.2.3 Wire Planes	9
1.2.4 Pad Plane	14
1.2.5 Electronics	15
1.3 Energy loss in material	17
1.3.1 Gas Properties	19
1.4 Pad Response Function	21
1.5 Radio Isotope Beam Factory (RIBF) Facility	24
1.6 Experimental Setup	25
1.7 Ancillary Detectors	27
1.7.1 Kyoto Multiplicity Trigger	27
1.7.2 Krakow KATANA Veto and Multiplicity Array	28
1.7.3 Active Veto Array	29
1.8 Data Acquisition (DAQ)	29
1.9 Trigger Condition	29
APPENDIX	33
BIBLIOGRAPHY	36

LIST OF TABLES

Table 1.1	An overview of the properties of the S π RIT TPC	4
Table 1.2	Wire plane properties	9
Table 1.3	Summary of range of GET electronics settings.	16
Table 1.4	21
Table 1.5	Primary and secondary beam properties produced in the S π RIT TPC experimental campaigns.	26
Table .1	List of runs for the analysis.	34

LIST OF FIGURES

Figure 1.1 Operation principle of the TPC	2
Figure 1.2 Overview of the S π RIT TPC	3
Figure 1.3 FC overview	5
Figure 1.4 FC overview 2	6
Figure 1.5 Schematic of the TPC system	6
Figure 1.6 Schematic of the electric connections relevant to the Field Cage system. The strip thickness is exaggerated in the figure to show the detail	7
Figure 1.8 On and off configurations of the gating grid.	11
Figure 1.10 Number of electrons produced in a single avalanche on an anode wire. Two different voltages were simulated using Garfield++ at 1470 V and 1214 V. The expected Polya distribution fit is also given in yellow.	13
Figure 1.11 Figure of the pad plane boards being glued to the top plate.	15
Figure 1.12 •	16
Figure 1.13 Schematic of the internals of the AGET chip from [1]	16
Figure 1.14 Readout structure of the AsAd boards and CoBo board structures. Also the relevant components of the DAQ system.	17
Figure 1.15 Energy loss of a $\beta\gamma = 3.6$ particle in Ar gas taken from [2]	18
Figure 1.16 Drift velocity of electrons in P10 gas.	20
Figure 1.17 A cartoon illustration of the charge distribution resulting from an electron avalanche on one wire and the projections of the distribution onto the two axis $\rho(x)$ onto the x-axis and $\rho(z)$ onto the z-axis. The orientation of the wire planes is flipped upside down to display the perspective better.	22
Figure 1.18 Experimental pad response function of many events for a crossing angle of $85^\circ < \theta \leq 90^\circ$	23
Figure 1.19 Overview of the RIBF, BigRIPS, and SAMURAI beamline.	25
Figure 1.20 Drawing of the experimental setup with the TPC inside of the SAMURAI magnet at 0° configuration.	26

Figure 1.21 Exploded views of Kyoto and KATANA arrays.	28
Figure 1.22 KATANA trigger box logic.	30
Figure 1.23 Master trigger logic.	31

CHAPTER 1

EXPERIMENT

1.1 Operational Principles of Time Projection Chambers

Time projection chambers are a class of detectors which reconstruct charged particles in all 3-dimensions. Here we will outline the physical principles involved in the TPC measurement and discuss the particular details of the TPC used in this thesis. Figure ?? depicts the inside of a TPC, specifically the field cage, which holds the detector gas and also sets up a constant electric field. As charged particles resulting from a heavy ion collision pass through the gas, electron-ion pairs are created from neutral gas molecules. The electrons are accelerated opposite to the electric field and the ions along with it. Since the mean free path of the electrons inside the gas is very small, they quickly collide with other gas molecules; slowing down, or even stopping the electron, which is then accelerated again, starting a repeating cycle of stop and go motion. This microscopic behavior manifests as a constant drift velocity when averaged over several gas collisions. The electrons drift up towards a set of wire planes eventually reaching a set of high voltage anode wires where they quickly accelerate in the presence of the high electric field, liberating more electron-ion pairs from the gas, creating an avalanche process to occur. The avalanche electrons eventually terminate either on the anode wire or the grounded pad readout plane, while the ions from the avalanche move slowly away from the anode wires, creating a large signal which is distributed over the pad-plane. The charge and timing information of these electrons are calculated from the induced signal measured by the electronics.

Two of the 3 coordinates are determined from the 2-dimensional charge distribution on the pad-plane. The third dimension comes from projecting the electrons back in time, utilizing the known constant drift velocity v_d . The distance the electron has traveled, d , – along the electric field direction– is calculated as $d = v_d \cdot t$, where t is the timing information of the signal in the electronics. The radius of curvature of the track is related to the magnetic rigidity, and therefore the

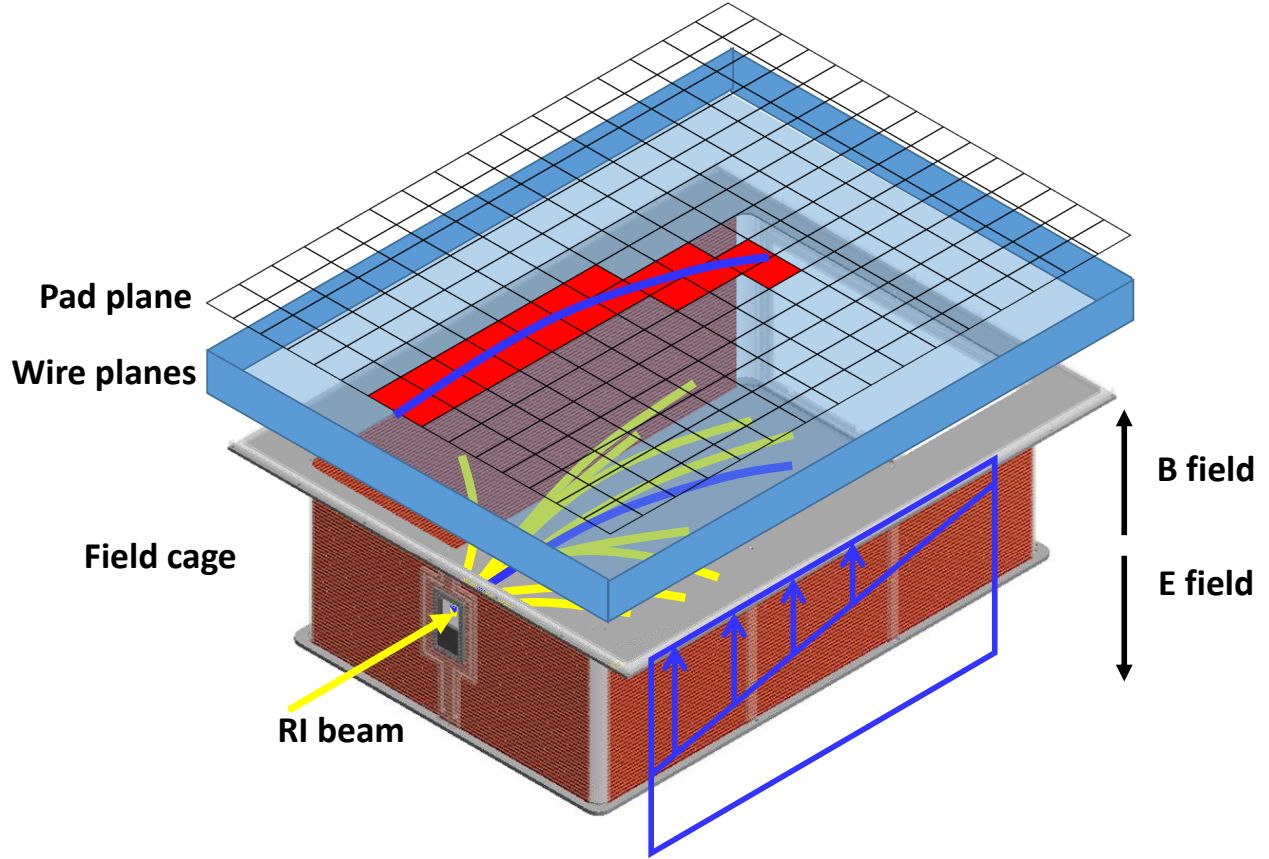


Figure 1.1: Operation principle of the TPC

momentum of each track. The energy loss deposited $\langle dE/dx \rangle$ is measured by the segmented charge sensitive pads on the pad-plane, in which each pad is connected to a channel in the electronics. Particle can be uniquely identified since each particles exists on unique rigidity and $\langle dE/dx \rangle$ lines, which will be discussed in latter sections. In this chapter we will discuss in more detail the process described above in the context of the specific TPC used in this thesis.

1.2 S π RIT TPC Overview

The Samurai Pion-Reconstruction and Ion Tracker Time Projection Chamber (S π RIT TPC) is a multi-wire proportional counter developed to measure pions and other light charge particles resulting from radioactive heavy ion collisions in fixed target experiments. The TPC is built on

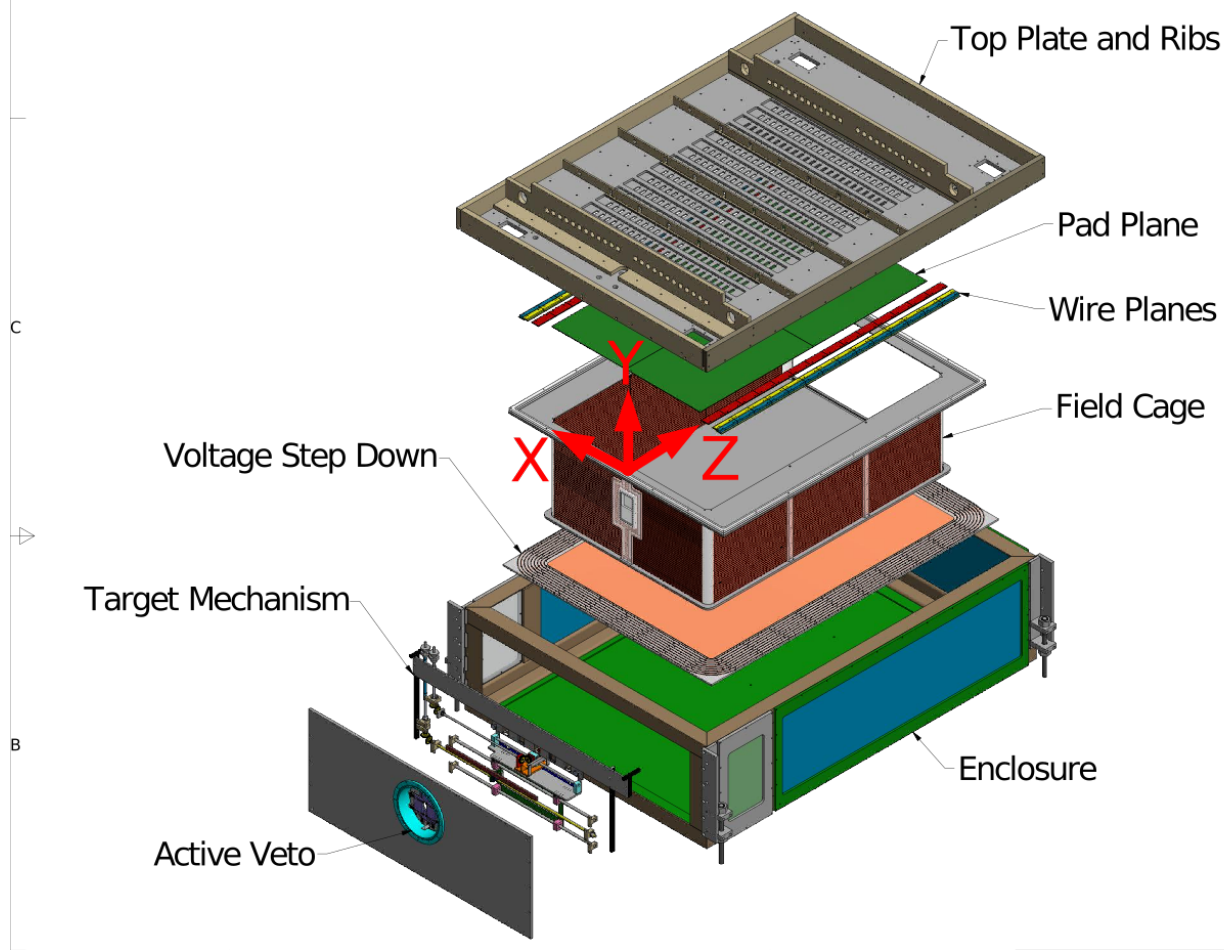


Figure 1.2: Overview of the S π RIT TPC

an aluminum angle iron skeleton with thin aluminum sheet walls in order to minimize neutron scattering and to allow for light charged particles to reach auxilliary detectors on the sides and downstream of the TPC. The S π RIT TPC was developed to fit inside the SAMURAI dipole magnet used at the Rare Isotope Beam Factory (RIBF) at RIKEN in Wako-shi, Japan [3]. The dipole gap limited the vertical space of the TPC to around 75 cm. More detail and specifications of the SAMURAI dipole magnet are given in [4].

A target mechanism allowed for up to 5 fixed targets to be mounted at anytime, with the ability to change targets on the outside of the TPC. The field cage contained the detector gas and set up the constant electric field, which was mounted to a large aluminum top plate, though electrically isolated by a lexan top perimeter ring with o-rings to provide as gas seal. The pad plane and wire

S π RIT TPC Overview	
Pad plane area	1.3 m x .9 m
Pad size	1.2 cm x .8 cm
Number of pads	12096 (112 x 108)
Gas composition	90% Ar + 10% CH ₄ (1 atm)
Multiplicity limit	200
dE/dx range	Z=1-3, π , p, d, t, He, Li
Drift length	50 cm

Table 1.1: An overview of the properties of the S π RIT TPC

plane structures are also mounted to the inside face of the top plate with the electronics being mounted on the outside face of the top plate. Several aluminum ribs were also mounted to provide extra rigidity to the top plate, keeping it flat to within 150 μ m, as measured by a precise laser measurement [5]. Holes on the top plate allowed for the readout of the individual charge sensitive pads on the pad plane, through surface mount pads which were connected through short cables to the electronics. The exploded drawing shown in Fig. 1.2 pictures all of the major internal components of the of the S π RIT TPC.

1.2.1 Field Cage

The field cage contains the detector gas and sets up a uniform electric field in which electrons can drift upwards toward the anode wires. It was designed to hang from the top plate and therefore needed to be of a lightweight construction. The materials needed to be thin to allow for light charged particle and neutrons to pass through without significant scattering for ancillary detectors.

The field cage was constructed from several panels of printed circuit boards (PCBs). The front of the field cage was made of two PCBs and each side was constructed from three PCBs, supported by Lexan pieces. The common PCB substrate material FR4, contains a bromine epoxy which can outgas and absorb electrons degrading the signal [6]. Therefore a halogen free material, Cryogenic-G10, was used for the board material. The field cage volume is isolated from the enclosure volume

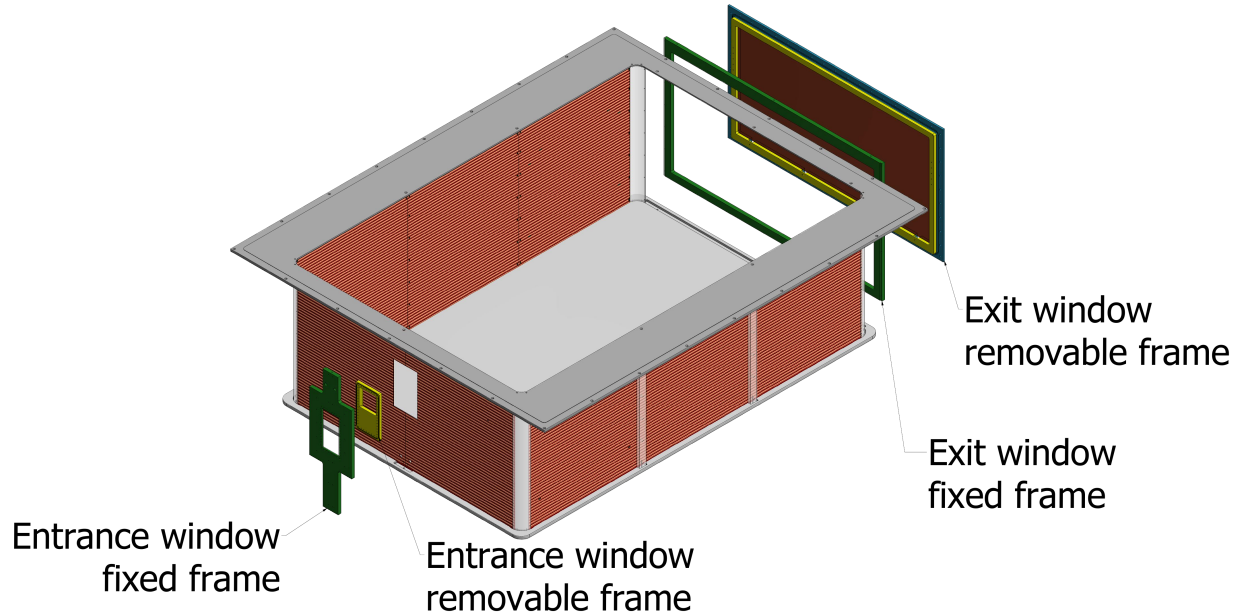


Figure 1.3: FC overview

of the TPC for the option to run two separate gasses, which may be useful when running explosive gasses such hydrogen. Instead of a downstream wall a, large, thin exit window was constructed, which consisted of a $10\text{ }\mu\text{m}$ Kapton window with evaporated aluminum strips, which was bonded to a removable Lexan frame. The PCB boards were epoxied, and screwed, into the cathode which was constructed from an aluminum honeycomb laminate, composed of two aluminum sheets bonded to an aluminum honeycomb core, providing a lightweight yet rigid structure. On the other end the boards were epoxied into an aluminum top perimeter which also served as the last ring in the TPC. Together with the cathode bottom, the field cage proved to be a rigid lightweight structure. A Lexan ring containing o-rings was placed in-between the top perimeter piece and the top plate of the TPC. Screws with nylon washers, and collars, were used to mount the top perimeter –and therefore the field cage– to the top plate; it also provided electrical isolation from the top plate. In this way the top plate could be removed and rotated with the field cage attached on without damaging any internal components.

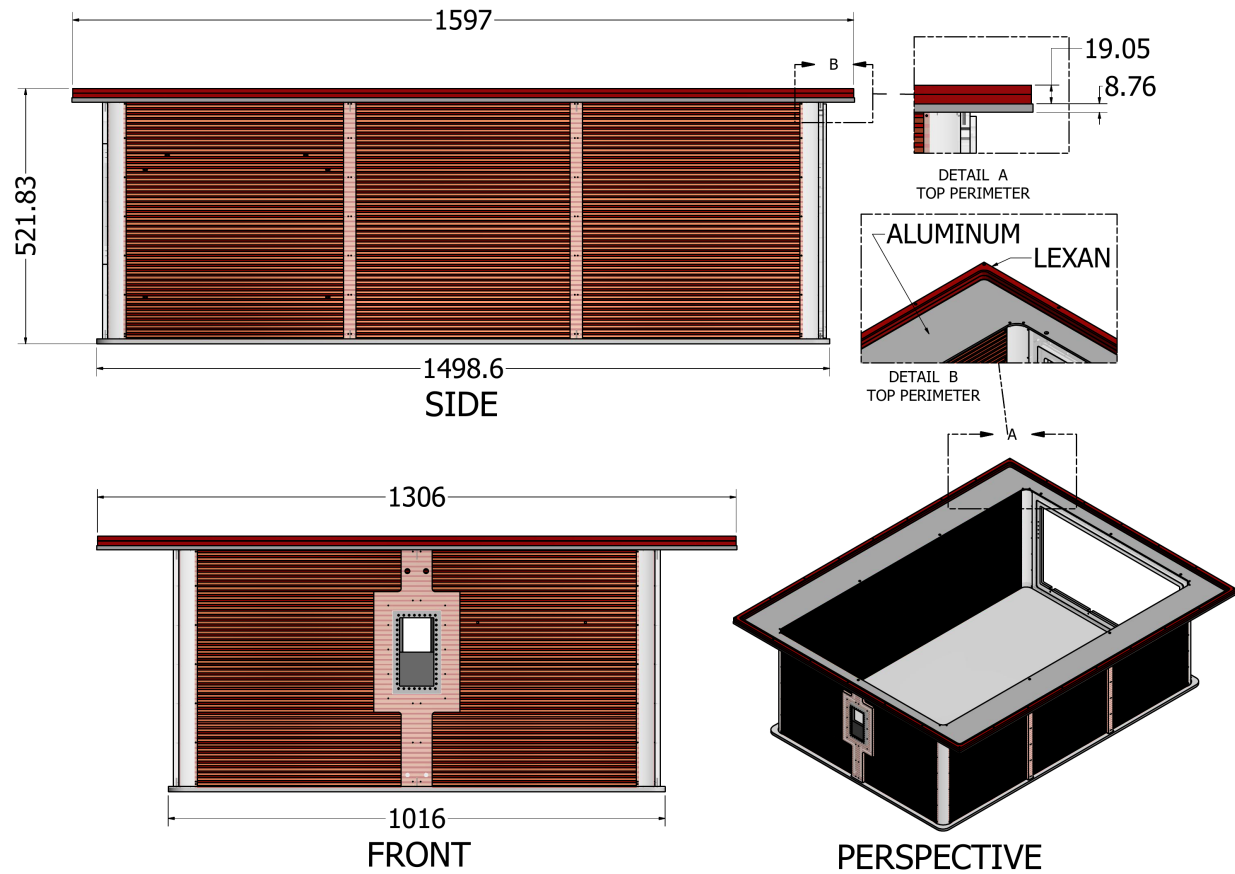


Figure 1.4: FC overview 2

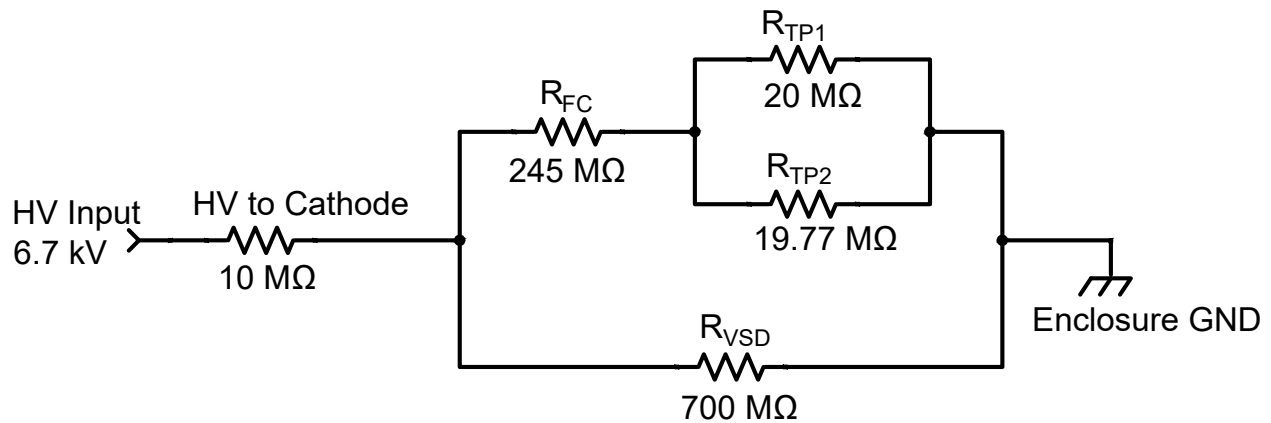


Figure 1.5: Schematic of the TPC system

Figure ?? shows the schematic of the effective resistances and capacitance of the TPC subsystem. The cathode is connected to the HV supply through a $10\text{ M}\Omega$ resistor and has an effective capacitance

to ground of 4 nF , C_{VSD} . The cathode voltage V_{cath} can be calculated as,

$$V_{cath} = \frac{V_{HV}}{1 + \frac{10}{((245+R_p)^{-1}+700^{-1})^{-1}}}, \quad (1.1)$$

where

$$R_p = (R_{TP1}^{-1} + R_{TP2}^{-1})^{-1}, \quad (1.2)$$

is the effective resistance of the last resistor, and V_{HV} is the high voltage supply; all resistor values are given in $\text{M}\Omega$.

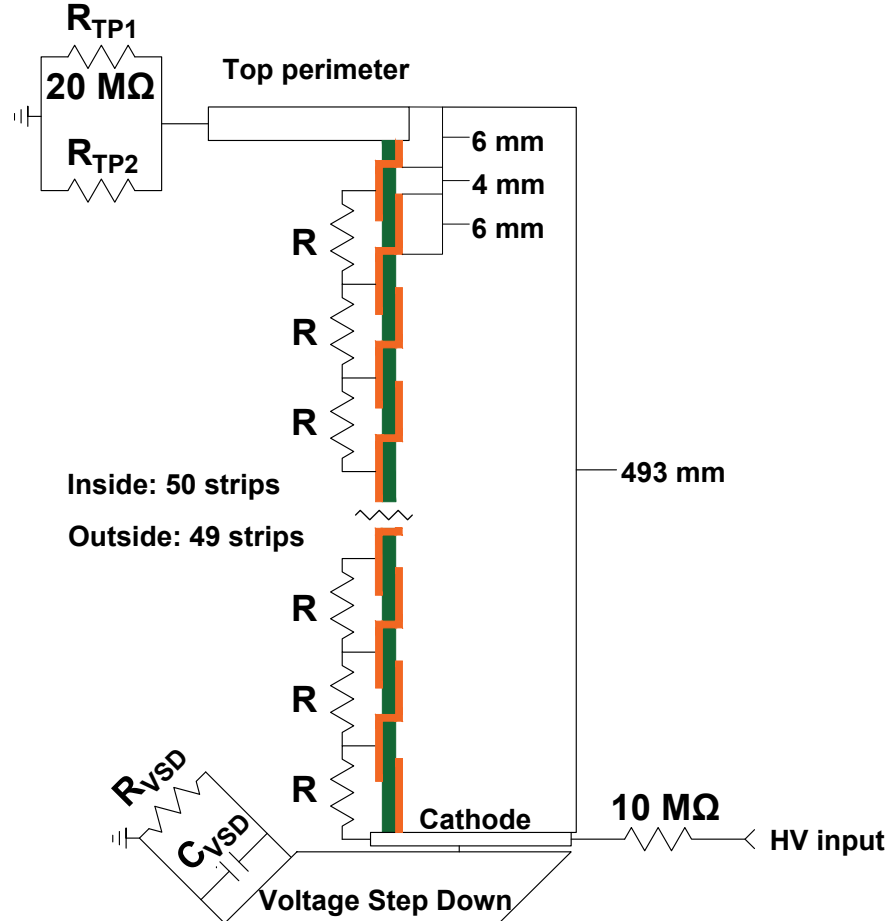


Figure 1.6: Schematic of the electric connections relevant to the Field Cage system. The strip thickness is exaggerated in the figure to show the detail

Figure 1.6 shows a schematic detailing the connections involved in the field cage walls. The field cage contains 50 inside copper strips and 49 outside copper strips. The strips are 6 mm in

width and spaced 10 mm apart. The strips on each board was connected to the adjacent strips on the adjacent boards. The interfaces were the side pieces met the front boards or back window are connected by G-10 corner pieces with conducting paint strips, which makes the strips into continuous rings around the whole field cage. The first inside strip is connected to the cathode, which is itself connected by an effective $5\text{ M}\Omega$ resistor (R) to the first outside strip. The first outside strip is connected through a via to the second inside strip. This pattern repeats until the last strip. The resistor chain creates a voltage divider in which each strip is separated by a constant difference voltage and a fixed distance, setting up a constant electric field. The last strip of the field cage is composed of a small inner strip (1.5 mm) on the PCB board and the top perimeter piece (4.5 mm) giving an effective thickness of 6 mm, the same as the other strip widths. The top perimeter is connected to electrical ground through a $20\text{ M}\Omega$ resistor (R_{TP1}) with the option to place an additional resistor (R_{TP2}) in parallel to tune the voltage of the top perimeter, as seen in Fig. 1.6.

The voltage on each strip, V_n , can be expressed as,

$$V_n = V_{cath} \frac{R_p + (50 - n)R}{49 \cdot R + R_p} \quad (1.3)$$

where $n = 1$ represents the index of the first inside strip, and $n = 50$ represents the index of the last inside strip, which is the same as the top perimeter voltage.

1.2.2 Voltage Step Down

The gap between the cathode and the ground of the enclosure is quite small. To prevent electric breakdown in the gas between this gap a series of concentric copper rings safely stepped down the voltage to ground in a controlled manner, reducing the chance of electric breakdown and sparking. There were 8 concentric rings with a $10\text{ M}\Omega$ resistors in between, creating a resistor chain which steps down the voltage each ring by approximately 1000 V each time. The first ring is the same voltage as the cathode and the last ring is connected to ground. All together the total resistance of the resistor chain is $700\text{ M}\Omega$.

1.2.3 Wire Planes

There are three wire planes that are mounted underneath the pad-plane. The wire plane closest to the pad-plane (4 mm) are the anode wires. The next plane (8 mm) is the ground plane or frisch grid, and the last plane (14 mm) is the gating grid. The gating grid is the first plane that electrons meet as they drift upward from the field cage volume towards the anode plane. The gating grid is operated as a gate, either allowing electrons and ions through, or blocking them entirely. The ground plane functions to shield the inside volume of the TPC from the high electric field surrounding the anode wires. The ground plane is the least interesting plane and is held to ground by shorting the plane to the enclosure through shorted BNC terminator on the outside of the TPC. We also use the ground plane to input a pulser which is used to spread the pulsed signal to all the pads on the TPC in order to calibrate the electronics of the TPC. This is done by replacing the shorted BNC with a 50Ω termination and injecting the pulser on the other end.

GET electronics settings

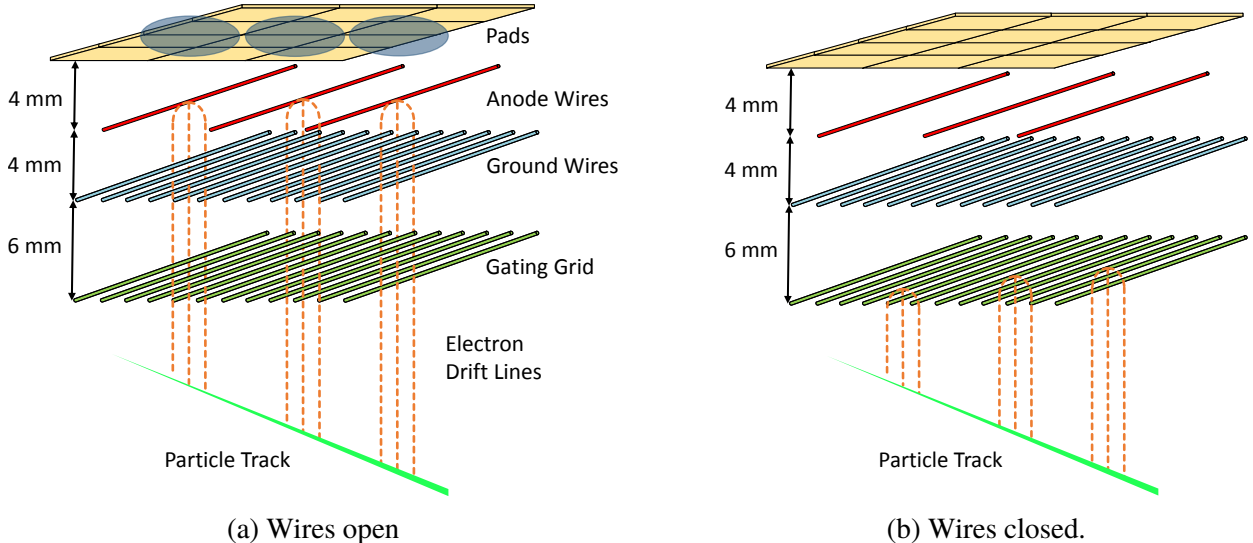
Plane	Material	Diameter μm	Pitch mm	Distance to pad-plane	Tension N	Voltage V
Anode	Au-plated W	20	4	4	0.5	1460
Ground	BeCu	75	1	8	1.2	0
Gating	BeCu	75	1	14	1.2	-110± 70

Table 1.2: Wire plane properties

In the open configuration, the gating grid is transparent to electrons coming from the field cage volume and also allows for ions to move from the avalanche region into the TPC volume. Typically the gating grid is held in the closed configuration, only opening it when the data acquisition trigger criteria is met. By keeping it always closed the electrons which come from the un-reacted beam are blocked, which if allowed to go to the anode wires, would quickly build up enormous amounts of positive ions, and would flood the volume of the field cage with space charge. We open the gating grid for about $11\mu\text{s}$ which is more than the time it takes for the electrons to drift one TPC volume. After this we close the gating grid to prevent the back-flow of ions from the avalanche

region from that event. Since ions move with a velocity much slower than that of electrons [7], the ions only move several μm in the time the gate is open; this allows for electrons to pass through while preventing the back-flow of ions into the FC volume.

Figure 1.8 shows a Garfield simulation of the drift lines of electrons in both the on and off configurations. In the on configuration, all the wires share the same average voltage, $V_{g.g.}$, in which the optimal voltage is selected for the case of 100% electron transparency. Figure 1.7a shows the electrons are allowed to drift completely through the gating grid all the way to terminate on the anode wires. In the off configuration, the reference voltage $V_{g.g.}$ remains the same, but alternating wires get an offset voltage of $\pm\Delta V$, so that the electric field produced by the voltage difference $2\Delta V$ between wires is great enough to block incoming electrons. Figure 1.7b shows this case were the electron drift lines are fully blocked terminating on the more positive wires. Opening the grid from this closed bi-polar mode is simply done by removing the offset voltage and allowing the two wires to short which equilibrates their charges, which is the steady state of the average reference voltage for 100% transparency.



Both configurations of the gating grid were measured and simulated. To measure the electron transparency were all wires share the voltage V_{avg} , the anode wire was lowered to 500 V and the beam was allowed to enter the field cage without any target put in. By lowering the voltage of the

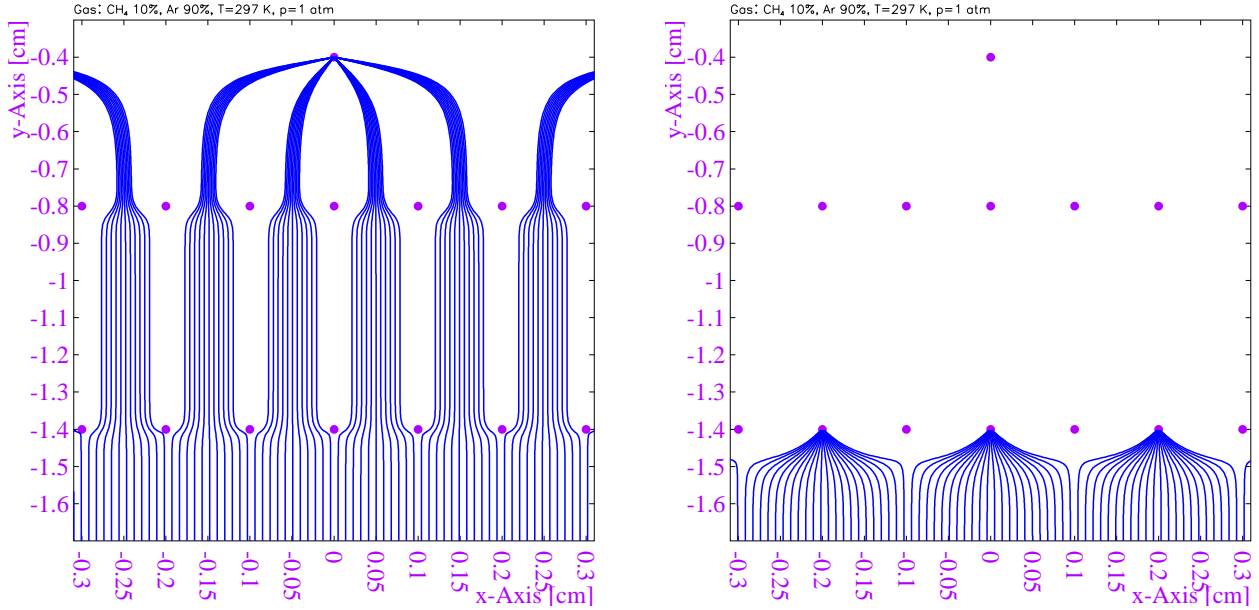
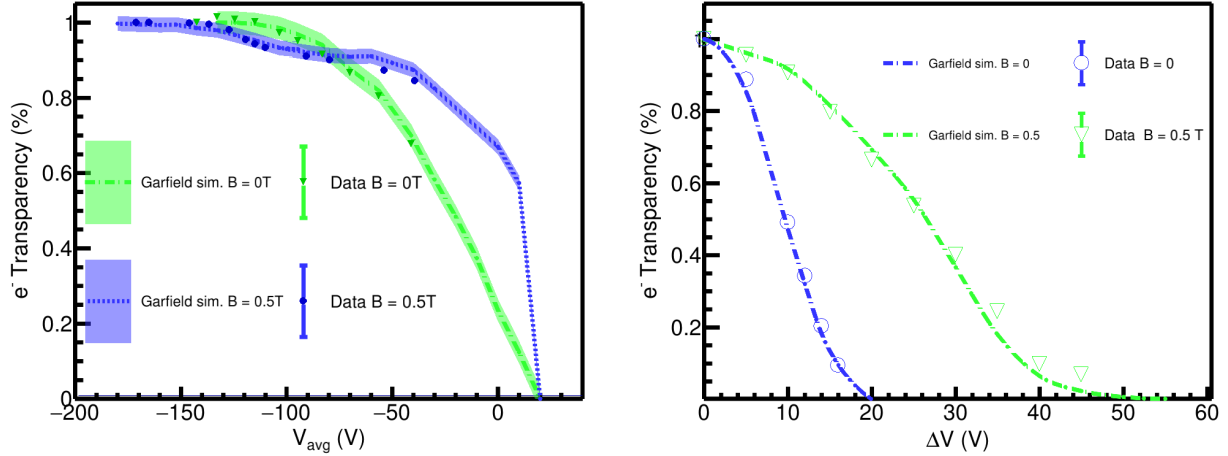


Figure 1.8: On and off configurations of the gating grid.

anode wires we could measure the large charge of the beam without saturating the electronics. The average charge deposited in the chamber could be measured as a function of V_{avg} ; changing the top plane resistor appropriately according to Eq. 1.7. Several runs were taken ranging from -198 V to -40 V , with and without the magnetic field. Theoretically the most negative value represents 100% electron transparency and was used as the reference run. The electron transparency, T , was defined as $T = \langle dE/dx \rangle / \langle dE/dx \rangle_{ref}$, where $\langle dE/dx \rangle_{ref}$ represents the average energy loss of the reference run. Figure 1.9a shows the measured transparency as a function of V_{avg} , as compared with the corresponding Garfield simulation. The average gating grid voltage used in the experiment was -171 V to ensure we were well within the 100% transparency region.

To measure the electron transparency as a function of the difference voltage ΔV , the average voltage was first set to 100% transparency, $V_{avg} = -171\text{ V}$, and the difference voltage was added or subtracted from alternating wires. Figure 1.9b shows the result of the simulation and experiment with and without the magnetic field. By introducing the magnetic field the required voltage to close the grid increases. In the experiment we selected the value of $\Delta V = 65\text{ V}$ to ensure we were well within the region of 0% transparency.



(a) Electron transparency for the conditions of all wires are the same voltage.

(b) Electrons transparency for the mode where adjacent wires have a voltage difference of $2\Delta V$.

The anode wires are made of very thin Gold plated Tungsten wires, about $20\text{ }\mu\text{m}$ in diameter. They are biased to high voltages around 10^3 V which creates a very high electric field very close to the anode wire. As the electron drifts towards the anode wire, it gains enough kinetic energy to knock out more electron-ion pairs in the gas which also go on to do the same; until they terminate on the anode wires or the pad plane. The amount of electrons produced depends on the anode wire voltage and the gas properties. The absolute gas gain was not experimentally measured but was calculated in a Garfield simulation. For the experimental data pertaining to this thesis, the anode wires were biased to two different voltages. We will refer to the voltage 1460 V as the “high voltage” and 1214 V as the “low voltage”. Only two sections were biased with the lower voltage setting due to a leakage around the end of the gating grid [5]. Figure 1.10 shows the electron distribution for the total number of electrons produced in a avalanche process created by a single electron. The distribution follows the expected Polya distribution, and the MC data in the simulation was fitted with a Polya function [7], which can be expressed as,

$$P(x) = A_0^{-1} \cdot \frac{A_1^{A_1}}{\Gamma(A_1)} \left(\frac{x}{A_0} \right)^{A_1-1} e^{\frac{-A_1 x}{A_0}}. \quad (1.4)$$

For the voltage of 1460 V the parameters of the fit are $A_0 = 903.9$ and $A_1 = 1.50$ and for the voltage of 1214 V the parameters are $A_0 = 150.0$ and $A_1 = 1.47$.

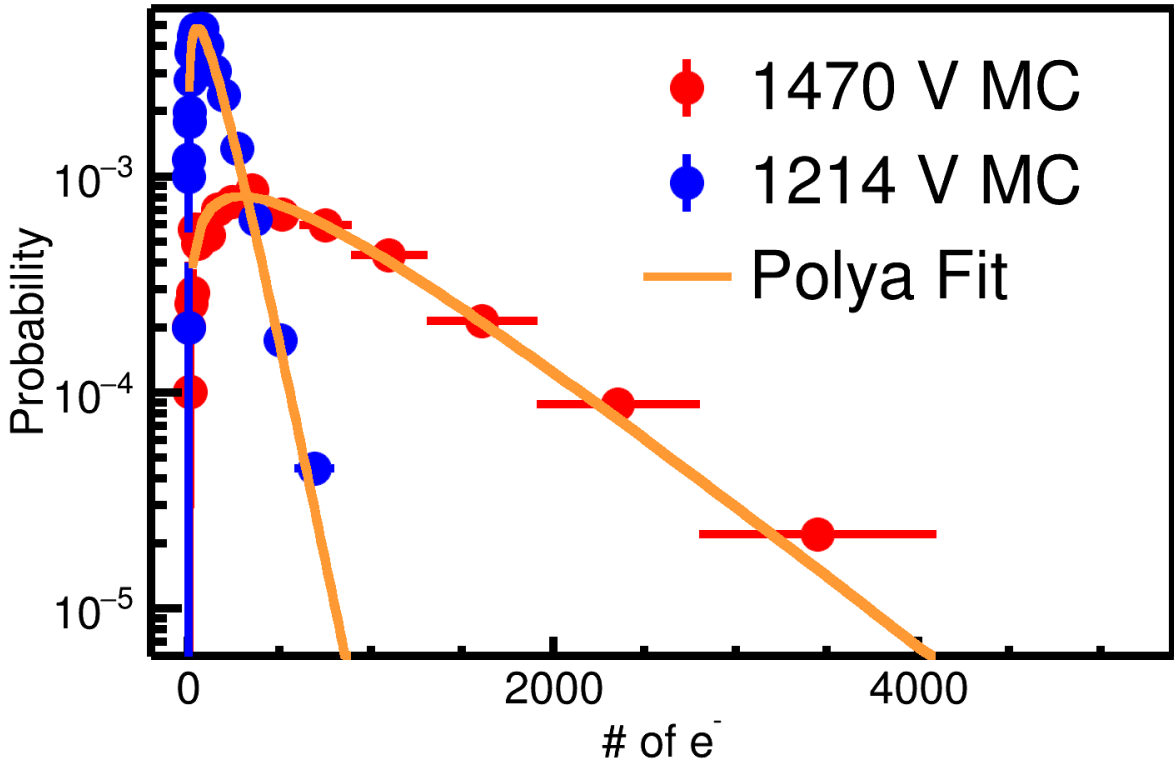


Figure 1.10: Number of electrons produced in a single avalanche on an anode wire. Two different voltages were simulated using Garfield++ at 1470 V and 1214 V. The expected Polya distribution fit is also given in yellow.

The main drift region is defined by the space between the gating grid and cathode voltages (Region 1), with a small drift region being defined by the space between the gating grid and the ground grid (Region 2), and the avalanche region is defined as between the ground grid and the anode grid. It is possible that the electric field in Region 1 and Region 2 can be matched but not required. To ensure the electric field is continuous across Region 1, the voltage of the top perimeter must be set properly by adjusting the value of the last resistor (R_{TP2}). We can imagine Region 1 is split into two virtual volumes, one defined as the volume between the cathode and the top-perimeter, and one defined between the top-perimeter and the gating-grid. The magnitude of the electric field in the region between the top-perimeter and the cathode, E_1 , is defined as,

$$E_1 = \frac{V_{g.g.} - V_{tp}}{y_{g.g.} - y_{tp}}, \quad (1.5)$$

where $V_{g.g.}$, V_{tp} , $y_{g.g.}$, and y_{tp} are the voltages and vertical y-positions of the gating-grid and top-perimeter respectively. The y-position here refers to the center of the electrodes. The magnitude of the electric field in the region between the top-perimeter and the cathode, E_2 , is defined as,

$$E_2 = \frac{V_{tp} - V_{cath}}{y_{tp} - y_{cath}}, \quad (1.6)$$

where V_{tp} , V_{cath} , y_{tp} , and y_{cath} are the voltage and vertical y-position of the top-perimeter and cathode respectively. The y-position of the cathode is defined as the face of the cathode. The condition for a smooth electric field across these two virtual volumes is defined as the solution to the equation $E_1 = E_2$. Substituting Eq. 1.3 for $V_{tp} - n = 50$ – we can solve for the effective resistance of the top perimeter R_p as,

$$R_p = 49 \cdot R \left(\frac{\frac{y_{g.g.} - y_{cath}}{y_{TP} - y_{cath}} - 1}{\frac{V_{cath} - V_{gg}}{V_{cath}}} \right), \quad (1.7)$$

where the relevant vertical dimensions are $y_{g.g.} - y_{cath} = 497.3$ mm and $y_{tp} - y_{cath} = 490$ mm.

The value of R_{TP2} can then be calculated from Eq. 1.2.

1.2.4 Pad Plane

The pad-plane is a multi-layer circuit board which is segmented into 11.5 mm x 7.5 mm charge sensitive pads; arranged in an array of 108 x 112 pads in the x and z-directions respectively, making 12096 pads in total. There is an insulating gap of 0.5 mm on each side separating the pads so that the effective area covered by the pads is 1344 mm x 864 mm. There is a via and trace coming from each pad, through the board, to the opposite side of the pad plane and is arranged in a surface pads which is readout by a surface mount SAMTEC connector. Figure 1.11 shows the pad plane boards being glued to the top plate and the holes which allow for the readout of pads. The pads were gold plated for excellent electric conduction properties.

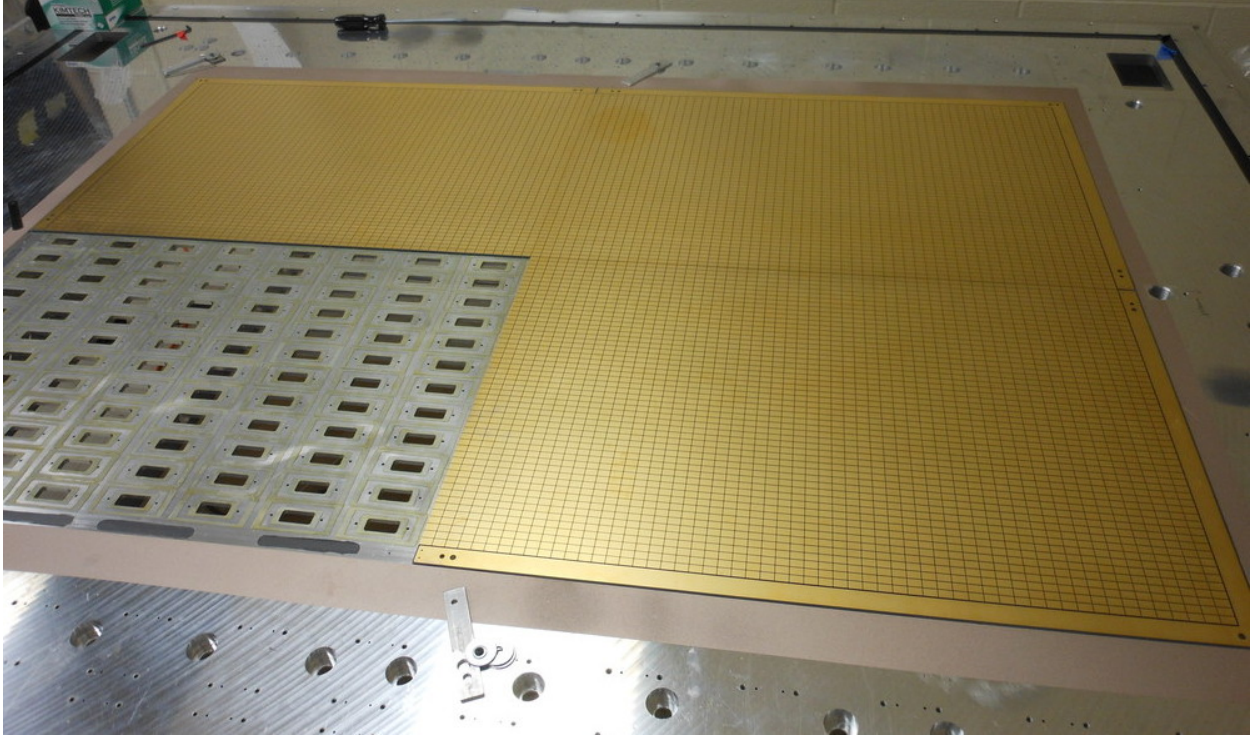


Figure 1.11: Figure of the pad plane boards being glued to the top plate.

1.2.5 Electronics

Signals in the S π RIT TPC are amplified and digitized by the recently developed Generic Electronics for TPCs (GET) [8]. Short cables transmit the signals from the surface mount connectors, through a circuit protection board called ZAP, to the inputs of the AGET chips which are mounted to the AsAd board as seen in Fig. 1.12. Each AGET chip services 64 pads (63 pads are connected in our case). Four AGET chips are mounted on one AsAd motherboard. Figure 1.13 is the schematic of each AGET chip which contains a charge sensitive pre-amplifier, several other stages of amplifiers, and a Switched Capacitor Array (SCA) with a maximum of 512 time buckets which operates in a circular readout buffer. The sampling frequency can be adjusted from 1 to 100 MHz. The gain of each AGET can be configured as 0.12, 0.24, 1.0, or 10 pC over the whole dynamic range, and the analog-to-digital converters (ADCs) on each AsAd board provides 12 bit resolution. The peaking times of the shaping amplifiers can be set to 69, 117, 232, 501, 720, or 1014 ns. In this experiment, the gain was set to the highest setting, 0.12 pC, the peaking time 117 ns, and the sampling frequency

25 MHz (resulting in 40 ns time buckets).

GET electronics settings	
ADC bit range	14 bits
Sampling frequency	1-100 MHz
Dynamic range	.12, .24, 1.0, 10pC
Peaking time	69,117,232,501,720,1014 ns
Time bucket range	512

Table 1.3: Summary of range of GET electronics settings.

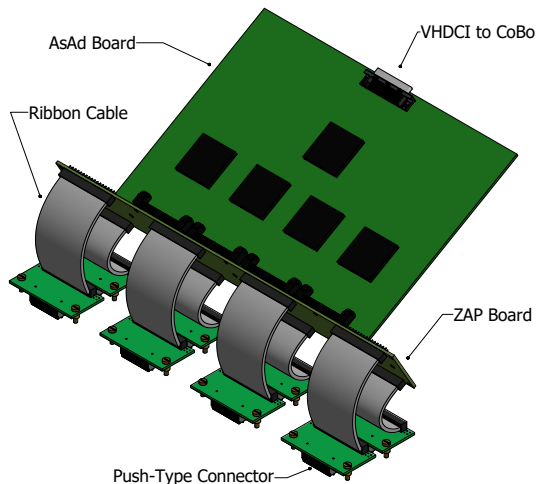


Figure 1.12: •

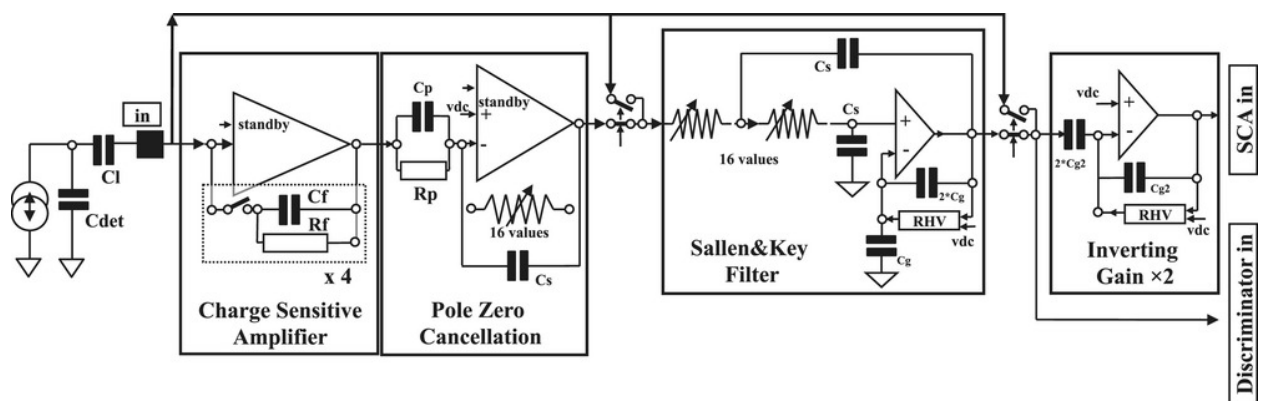


Figure 1.13: Schematic of the internals of the AGET chip from [1]

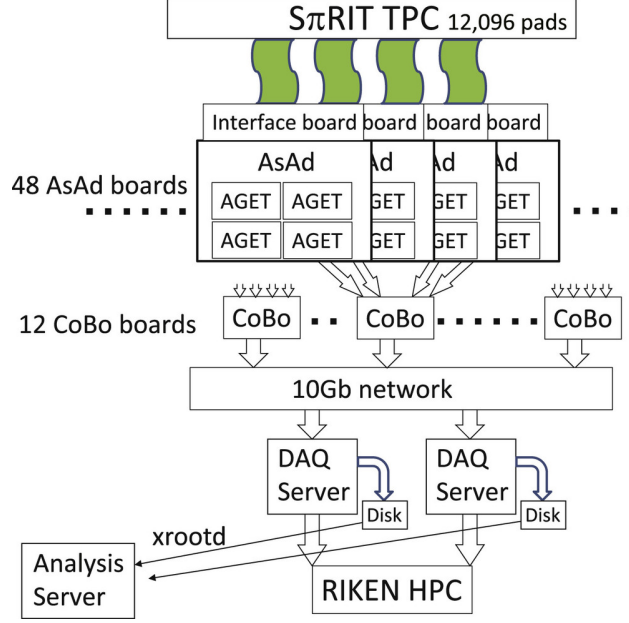


Figure 1.14: Readout structure of the AsAd boards and CoBo board structures. Also the relevant components of the DAQ system.

After each AsAd board has digitized the data it is sent to the Concentration Boards (CoBo). Each CoBo board can concentrate the data from 4 AsAd boards. The Multiplicity, Trigger, and Time module (MuTanT) [8] provides the common trigger signal for all CoBo boards. Each board sends the data to the DAQ server which writes to disk the data from each board, which was handled by two separate DAQ servers; saving to one common analysis server. The data could then be analyzed using the RIKEN High Performance Computing (HPC) cluster or moved to the NSCL or MSU cluster for analysis. The Aget 2.0, asad 2.1, and cobo 1.0 firmware versions were used in this analysis.

1.3 Energy loss in material

The average energy loss in a material can be described by the Bethe-Bloch equation,

$$\frac{dE}{dx} = \frac{4\pi N Z^2 e^4}{mc^2 \beta^2} \left(\ln \frac{2mc^2 \beta^2 \gamma^2}{I} - \beta^2 \right), \quad (1.8)$$

where N is the number density of electrons in the medium, e the elementary charge, mc^2 is the rest mass of the electron, Z is the charge of the traversing particle, I is the mean excitation energy

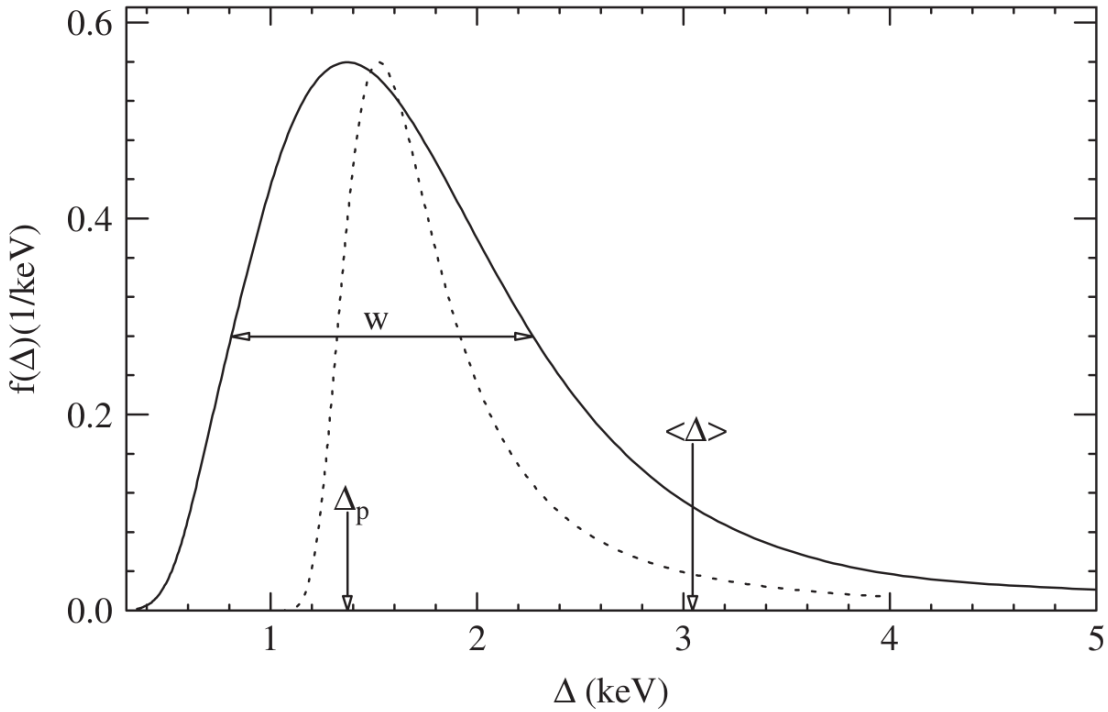


Figure 1.15: Energy loss of a $\beta\gamma = 3.6$ particle in Ar gas taken from [2]

of the medium, and β is the velocity of the particle [7]. Yet there is a large variation in energy loss around this mean value. The statistical variation of energy loss in a material was described by Landau [9] and later better described by Shulek [10] and Bichsel [11]. In both approximations it is described by a most probable energy loss value, with a long, high-energy loss tail. The solid curve in Fig. 1.15 shows the energy loss distribution in Ar gas for a proton with momentum $3.4 \text{ GeV } c^{-1}$. The dashed line is the distribution under the Landau assumptions. The mean energy loss $\langle \Delta \rangle$ is significantly shifted from the most probable value Δ_p , due to the long high energy tail. Because of this long tail, for a finite set of energy loss measurements along a given track, the fluctuation of the mean value energy loss as an observable is a very unreliable. The most probable energy loss is the better observable which can be obtained either through fitting of the observed distribution or through the truncated mean method.

The truncated mean is the average mean value calculated after throwing away the top fraction of the highest energy loss entries. This approximates the most probable value without performing

a fit to a known distribution. The set of n observed energy loss values, Δ_i/x , in a given track are sorted from smallest to largest value. The truncated mean C , is calculated from the reduced set of points $n_t = f_r n$ as,

$$C = \frac{1}{n} \sum_i^{n_t} \Delta_i/x, \quad (1.9)$$

where f_r is the cut off fraction; in this thesis, a value of 0.7 was used.

1.3.1 Gas Properties

The gas used was a mixture of 90% Ar and 10% Methane (CH_4) by volume (P10 gas), and operated just under atmospheric pressure 1 atm. The gas was continually flowed through the field cage and exited into the enclosure volume, finally passing through a bubbler to atmosphere. The gas purity was monitored with an oxygen and water monitor which are the two most concerning contaminants. The water never exceed ??? ppm and the oxygen level never exceeded ??? ppm. Figure 1.16 shows the drift velocity of P10 gas at 1 atm (760 Torr) as a function of the reduced electric field value given in units of $\text{V cm}^{-1} \text{Torr}^{-1}$. Operating near the peak value of the drift velocity curve minimized the change in the drift velocity as the effective field slightly changes due to slight variations in the pressure. The electric field in the experiment was 125 V cm^{-1} at 760 Torr, giving a reduced electric field $0.17 \text{ V cm}^{-1} \text{Torr}^{-1}$.

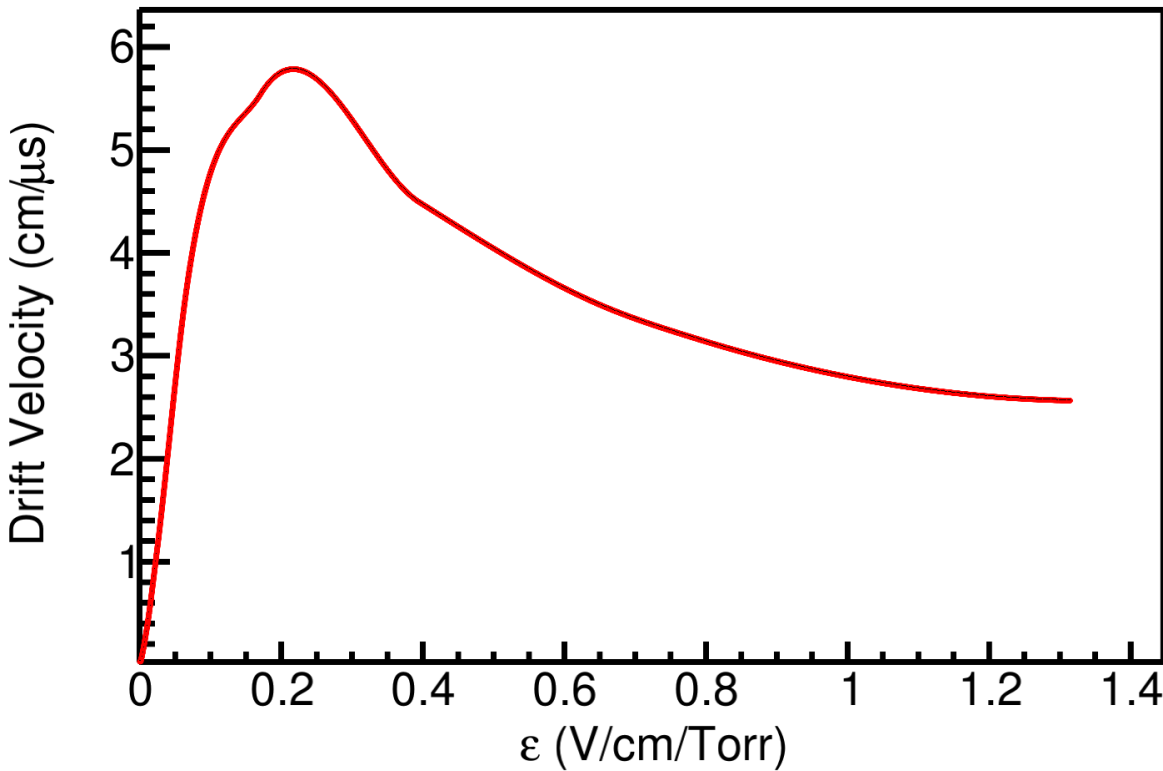


Figure 1.16: Drift velocity of electrons in P10 gas.

The general formula for the drift velocity, $d\vec{x}/dt$, of an electron in the presence of electric and magnetic fields, \vec{E} and \vec{B} , can be expressed in the Langevin equation as,

$$\frac{d\vec{x}}{dt} = \frac{\mu}{1 + (\omega\tau)^2} \left(\vec{E} + \omega\tau \frac{\vec{E} \times \vec{B}}{|\vec{B}|} + \omega^2\tau^2 \frac{\vec{E} \cdot \vec{B}}{|\vec{B}|^2} \vec{B} \right), \quad (1.10)$$

where μ is the signed drift velocity, ω is the cyclotron frequency, and τ is the collision parameter for a particular gas [7].

Several properties of the gas were also simulated in Garfield such as the longitudinal and transverse diffusion, σ_l and σ_t respectively, and the electron and ion drift velocities, v_d and v_i respectively for the experimental electric field of 125 V cm^{-1} ; summarized in Table 1.4.

ADD THE VALUES OF TAU AND MU HERE

Gas properties	σ_t (cm $^{-1/2}$)	σ_l (cm $^{-1/2}$)	v_d (cm μ s $^{-1}$)	v_i (cm μ s $^{-1}$)	G_h	G_l
	0.024	0.034	5.43	2.05×10^{-4}	903	150

Table 1.4

1.4 Pad Response Function

Each electron avalanche produces an two-dimensional image charge on the pad plane, as shown in the cartoon in Fig. 1.17, where the projection of the charge distribution onto the x and z axis of this distribution are labeled as $\rho(x)$ and $\rho(z)$ respectively. If $\rho(x, z)$ represents the charge distribution on the pad-plane, the total charge observed a particular pad, Q , is expressed as,

$$Q(x_o, z_o) = \int_{z_o - \frac{l}{2}}^{z_o + \frac{l}{2}} \int_{x_o - \frac{w}{2}}^{x_o + \frac{w}{2}} \rho(x - x_o', z - z_o') dx dz, \quad (1.11)$$

where x_o and z_o represent coordinates of the center of that pad, x_o' and z_o' are the coordinates of the avalanche, w is the width, and l is the length of the pad. The total charge observed for a given track is a superposition of all avalanches on all the anode wires. Typically in a TPC, the charges on each pad are grouped into clusters, and it is practical to cluster in only one direction. Therefore we will speak about the marginal probability distribution over a given layer of pads (x-distribution), or row of pads (z-distribution). The marginal distribution for a given layer can be written as,

$$\rho_x(x) = \int_{z_o - \frac{l}{2}}^{z_o + \frac{l}{2}} \rho(x, z) dz, \quad (1.12)$$

and over a given row can be written as,

$$\rho_z(z) = \int_{x_o - \frac{w}{2}}^{x_o + \frac{w}{2}} \rho(x, z) dx. \quad (1.13)$$

By substituting the variables $\lambda_x = x - x_o'$, and $\lambda_z = z - z_o'$, we can express the charge distribution independent of the avalanche location. The Pad Response Function (PRF) along the x-direction of a given layer can be written as,

$$P_X(\lambda_{x_o}) = \frac{\int_{\lambda_{x_o} - \frac{w}{2}}^{\lambda_{x_o} + \frac{w}{2}} \rho_x(\lambda_x) d\lambda_x}{\int_{-\infty}^{\infty} \rho_x(\lambda_x) d\lambda_x}, \quad (1.14)$$

where $\lambda_{x_o} = x_o - x_o'$; in a similar manner for the situation we cluster along the z-direction of a given row the PRF can be written as,

$$P_Z(\lambda_{z_o}) = \frac{\int_{\lambda_{z_o} - \frac{l}{2}}^{\lambda_{z_o} + \frac{l}{2}} \rho_z(\lambda_z) d\lambda_z}{\int_{-\infty}^{\infty} \rho_z(\lambda_z) d\lambda_z}, \quad (1.15)$$

where $\lambda_{z_o} = z_o - z_o'$.

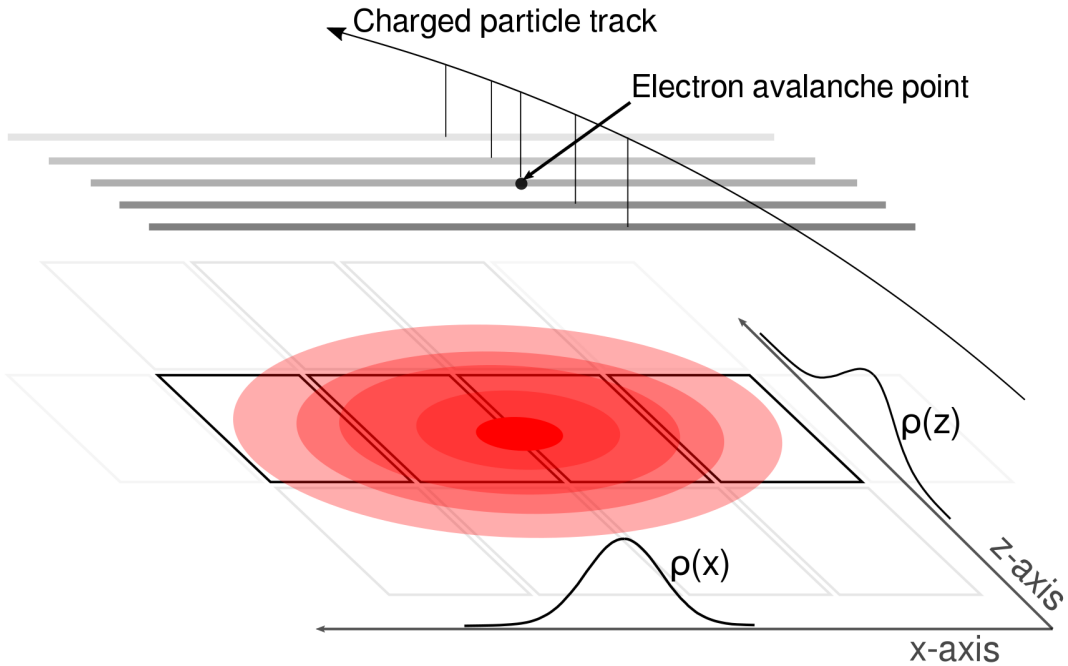


Figure 1.17: A cartoon illustration of the charge distribution resulting from an electron avalanche on one wire and the projections of the distribution onto the two axis $\rho(x)$ onto the x-axis and $\rho(z)$ onto the z-axis. The orientation of the wire planes is flipped upside down to display the perspective better.

Gatti [12] derived a semi-empirical formula for the charge distribution in a simple multi-wire

TPC given as,

$$PRF_{\text{Gatti}}(\lambda) = \frac{K_1}{K_2 \sqrt{K_3}} [\arctan(\sqrt{K_3} \tanh[K_2(\frac{\lambda}{h} + \frac{w}{2h})]) - \arctan(\sqrt{K_3} \tanh[K_2(\frac{\lambda}{h} - \frac{w}{2h})])] \quad (1.16)$$

where w is the width of the pad, h is the distance of the anode plane to the pad plane, and λ is the distance of the pad center to the avalanche point. It is a single parameter equation where the two parameters $K_1 = \frac{K_2 \sqrt{K_3}}{4 \arctan(\sqrt{K_3})}$ and $K_2 = \frac{\pi}{2} \left(1 - \frac{\sqrt{K_3}}{2}\right)$ depend on the parameter K_3 , which is a function of the ratio of the anode wire diameter to the distance of the anode wires to the pad plane. K_3 can be looked up in a graph in [7] and [12].

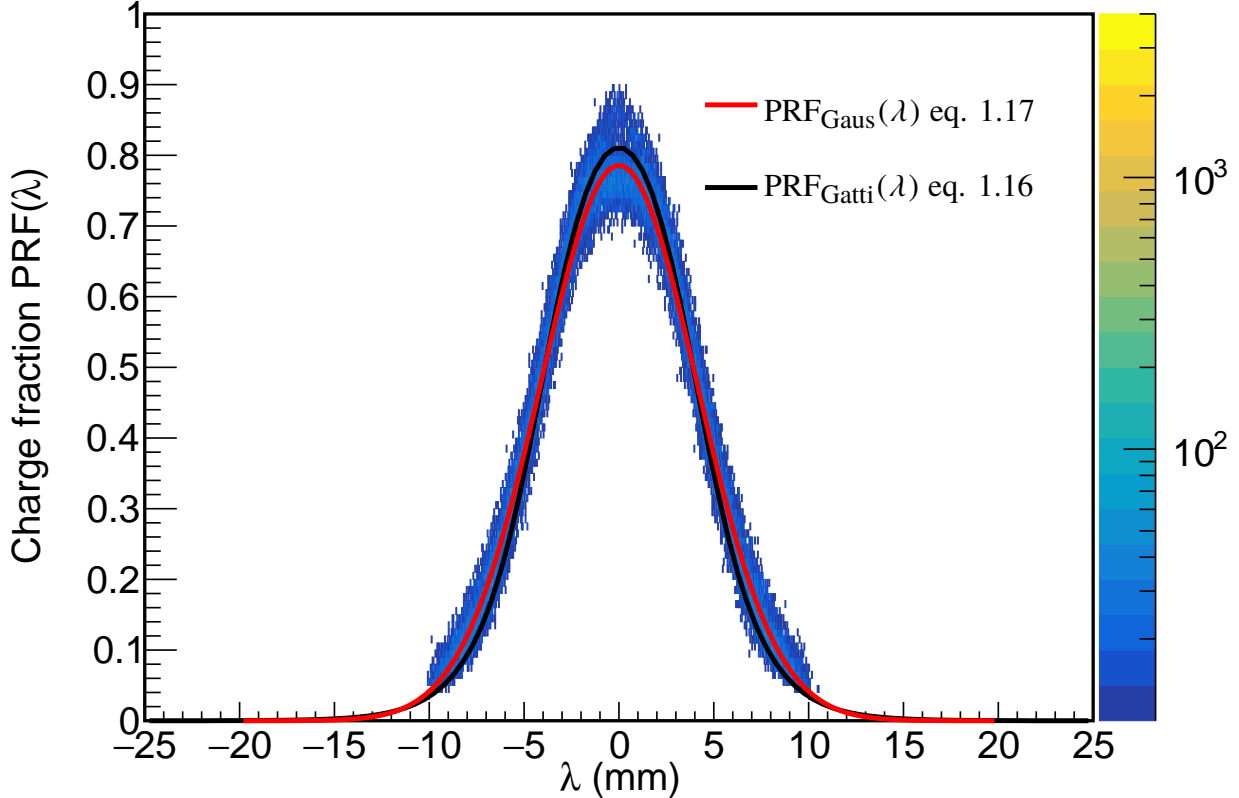


Figure 1.18: Experimental pad response function of many events for a crossing angle of $85^\circ < \theta \leq 90^\circ$.

Since we take the marginal distributions only along one layer or row of pad, correlations are introduced in the PRF from adjacent layers or rows which cause slight deviations from the expected Gatti distribution. Also, analytic PRFs only exist for classical multi-wire TPCs. For these reasons

it is useful to experimentally measure the PRF and fit it with an empirical function, typically a Gaussian, to describe its behavior. The method for extracting the experimental PRF will be discussed latter, but by averaging over many events in the experimental data, the resulting PRF for the S π RIT TPC is shown in Fig. 1.18. Here we see the deviations from the expected analytic Gatti distribution (black curve), whereas fitting with a two parameter Gaussian function (red curve) gives a better description of the data, Eq. 1.17, with the two parameters being the normalization coefficient, N_0 , width σ , and with a mean value assumed to be 0.

$$PRF_{\text{Gaus}}(\lambda) = N_0 e^{\frac{-\lambda^2}{2\sigma^2}} \quad (1.17)$$

1.5 Radio Isotope Beam Factory (RIBF) Facility

The primary and secondary beams were produced at the Radioactive Isotope Beam Factory (RIFB) facility at RIKEN, in Wako-shi, Japan. The RIBF facility starts with two primary beam types, ^{132}Xe and ^{238}U , which are produced by an ion-source and accelerated to progressively higher kinetic energies by 1 linear accelerator (RILAC), and 4 different cyclotrons (RRC, fRC, IRC, and SRC), until they reach a beam energy of 345 MeVA. Figure 1.19 shows the later stages of the cyclotrons and the following beam lines they feed into.

After the SCR, the primary beams impinge on a rotating 3 mm Be target which produces many different species by fragmentation. These fragments are then separated by the BigRIPS spectrometer which is tuned to the particular secondary fragment of interest. This is accomplished through several dipole magnets, slits, and wedge degraders. The resulting secondary beam is not pure and the purity depends on the capability of BigRIPS to deliver the secondary beam of choice and the primary beam used.

In these set of experiments several beams were produced with varying intensities and purities. Table 1.5 summarizes the average qualities of the 4 secondary beams produced in the two experimental campaigns where most beams were delivered with an intensity of 10 kHz. The BigRIPS

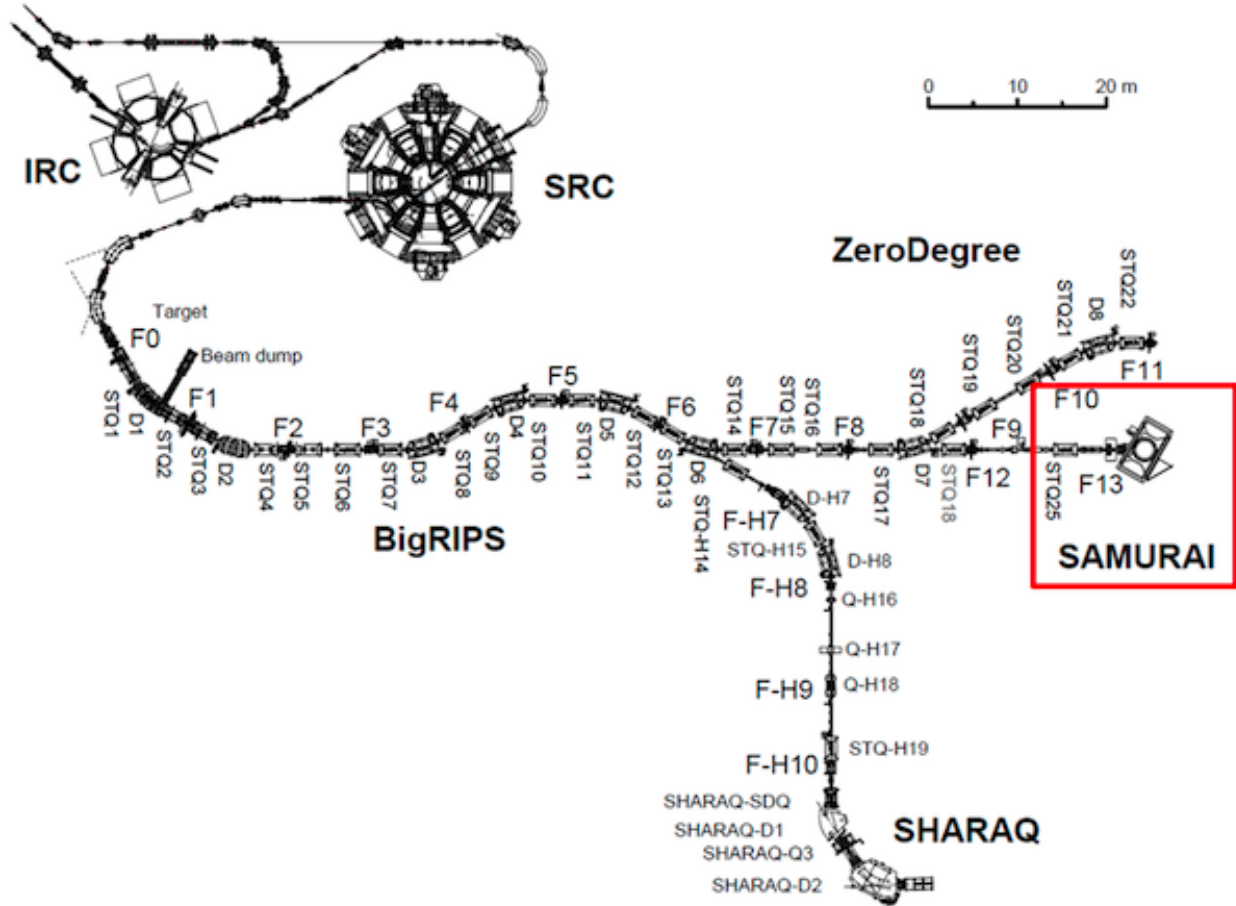


Figure 1.19: Overview of the RIBF, BigRIPS, and SAMURAI beamline.

separator had beam tracking elements which allowed for further identification of each individual beam produced. Allowing for a selection on the events corresponding to the secondary beam of choice CITE HERE.

1.6 Experimental Setup

The $S\pi$ RIT TPC was designed to fit exactly into the dipole gap of the dipole magnet at the end of the BigRIPS beam line. Figure 1.20 shows a drawing of the $S\pi$ RIT TPC inside of the SAMURAI magnet chamber which was rotated to the 0° configuration. Typically the SAMURAI (Superconducting Analyzer for Multi-particles from Radioisotope beams) is operated under vacuum as a large-acceptance multi-particle spectrometer for radioactive-beam experiments. This magnet

Primary Beam	Secondary Beam	Energy at mid target MeV A	Intensity kHz	Purity (%)
^{238}U	^{132}Sn	269.2	9.5	54
^{238}U	^{124}Sn	270.3	9.1	10
^{124}Xe	^{112}Sn	270.4	7.6	48
^{124}Xe	^{108}Sn	269.3	7.5	52

Table 1.5: Primary and secondary beam properties produced in the S π RIT TPC experimental campaigns.

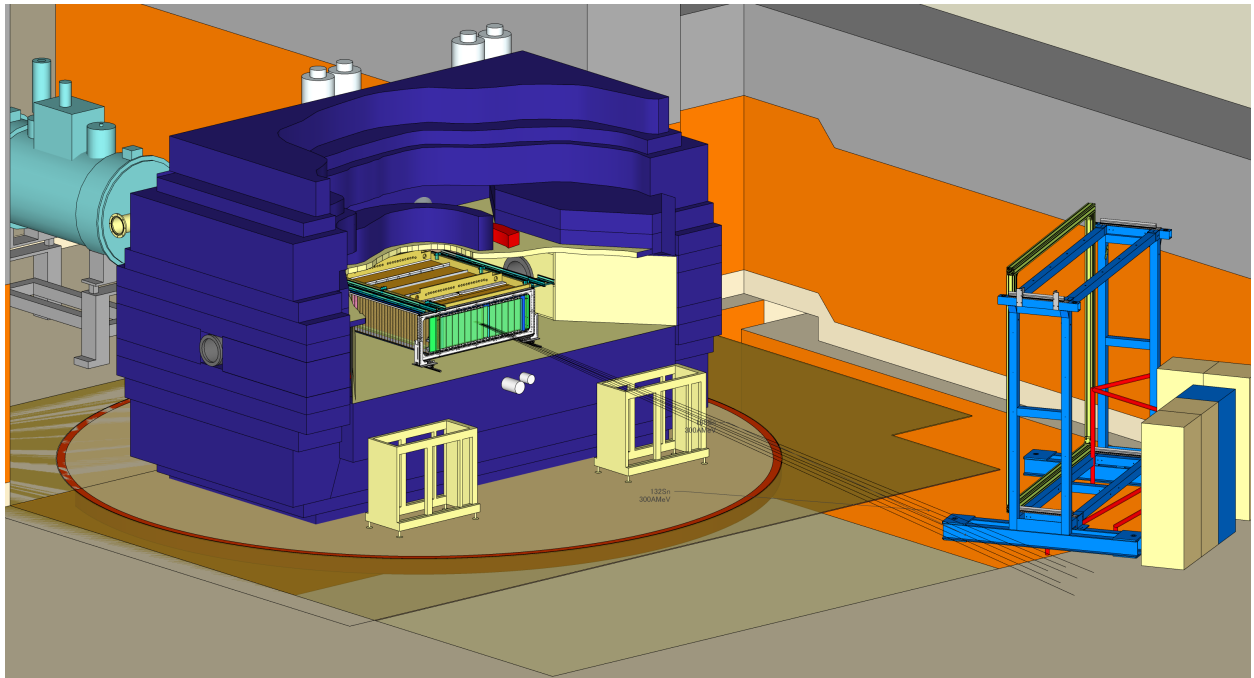


Figure 1.20: Drawing of the experimental setup with the TPC inside of the SAMURAI magnet at 0° configuration.

can reach magnetic fields up to 3 T at the center of the pole gap and was operated at 0.5 T for these sets of experiments. The space between the magnetic pole faces is further complicated by large bolts which protrude from the pole faces. These bolts secure the vacuum chamber to the magnet which is not practically removable; though the inside of the magnet was not operated under vacuum. This required an extensive rail system and support frame to slowly slide in the TPC over the bolts, finally raising the TPC several cm to the final height.

The height of the TPC was roughly aligned with a self-leveling laser system to match the center

of target with the center of the beam line. Once the TPC was adjusted to the final location, the position of the TPC was measured in fine detail with a the VStars-N photogrammetry system [13]. Small highly reflective targets were placed all over the TPC both inside and out and pictures were taken with a calibrated lens and camera system. Using the commercial software provided the set of different camera perspectives was reconstructed into a 3-dimensional point cloud of all the targets. Since the magnet was also measured with the same system after installation, we can match the two systems to get the absolute position of the TPC, and its internal components, relative to the magnet frame. The position resolution of this type of system was estimated to be around $200\text{ }\mu\text{m}$ for each coordinate, which is much more precise than needed or Show data.

PUT HERE THE MAGNET FRAME COORDINATE PUT HERE THE TPC FRAME COORDINATE DEFINITION

1.7 Ancillary Detectors

Several ancillary detectors were placed inside and outside of the S π RIT TPC to facilitate in making the trigger for the experiment. Placing detectors around the TPC was one of the important considerations we made when designing the TPC. A brief description of each detector system is given here with particular focus on how the experimental trigger was made.

1.7.1 Kyoto Multiplicity Trigger

As seen in Fig. ??, the Kyoto Multiplicity Array consists of two arrays of plastic scintillating bars on each side of the TPC, each consisting of 30 bars. The entire TPC structure was designed so that light charged particles could easily pass through the field cage and side walls of the TPC enclosure. In this way the number of tracks passing through the sides of the TPC could be measured by this array. In heavy ion collisions the more central a nuclear collision is, the more nucleons participate in the collision, resulting in a higher observed track multiplicity. It is this correlation between the number of tracks and centrality of the collision that makes the Kyoto Array sensitive to the

centrality of events. It is more likely that in very central collisions more tracks are going to the peripheral angles and measured by the Kyoto array. In the experiment the trigger selection criteria was $n_{Kyoto} > 4$, where n_{Kyoto} is the total number of tracks measured by both arrays. The Kyoto array proved to be a good trigger for selecting on very central events as will be discussed in later sections.

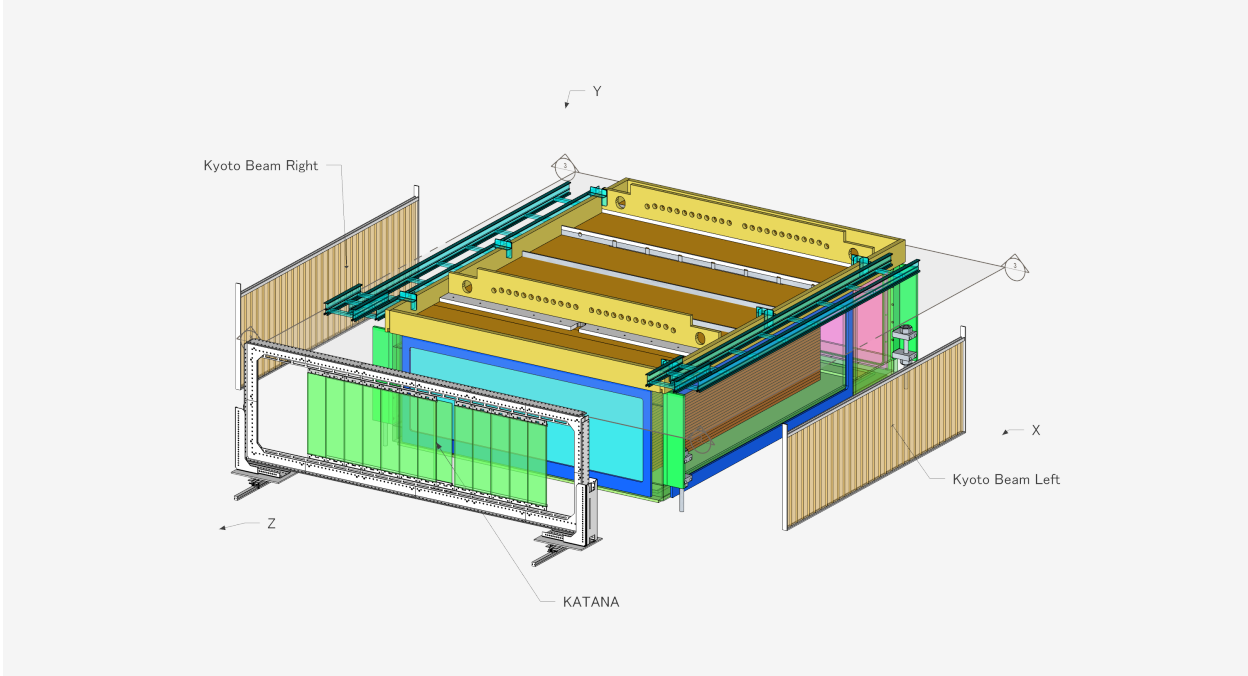


Figure 1.21: Exploded views of Kyoto and KATANA arrays.

1.7.2 Krakow KATANA Veto and Multiplicity Array

Also shown in Fig. ?? is the Krakow KATANA array, which consists of 12 plastic scintillating bars mounted to the downstream wall of the TPC enclosure. Three of the 12 bars were thin and operated as a beam veto in the event the beam did not make a nuclear collision with the target; this was a majority of the time. The 9 other bars operated as an additional multiplicity array similar to the Kyoto array. Since most of the particles are focused forward into a cone in the laboratory frame, it was found the condition on the Kyoto array was sufficient to trigger on central events; thus the

KATANA array was used in primarily the beam veto mode. This was accomplished by positioning the array so that the expected position of the beam exiting the TPC would be centered on the three thin paddles. The threshold of the veto paddles were set so that the charge of a particle passing through, Z , would veto any event that satisfied $Z > 20$, where the charge of the Sn beam is $Z = 50$.

1.7.3 Active Veto Array

The beam was tuned by two sets of quadrupole magnets, STQ 1 and STQ2 (as seen in Fig. 1.19), so that the beam spot was focused on the TPC target location. Because of the inherent angular dispersion of the beam there still were incoming beam events which significantly deviated from the target location. To veto these type of events an active veto array was set at the entrance of the TPC consisting of four small scintillating bars arranged to be slightly larger than the target size. The threshold was set so that any beam particle which passed through any of the bars it would send a trigger signal to not trigger the system since the beam path would not be on target but on some other material inside the TPC.

1.8 Data Acquisition (DAQ)

The Data AcQuisition (DAQ) consisted of three different systems. The RIBFDAQ system served as the master DAQ for the BigRIPS beam identification DAQ, the TPC DAQ, the NeuLAND neutron wall DAQ, and the Kyoto Array DAQ systems. The TPC DAQ was handled by the NARVAL framework to readout the GET electronics for the S π RIT TPC. A General Trigger Operator (GTO) trigger was supplied to each DAQ synchronizing the subsystems.

1.9 Trigger Condition

Signals from all of the auxiliary detectors were combined into several logic combinations to form a trigger logic for triggering the data acquisition (DAQ) to record data. An upstream scintillating

bar formed the start counter signal, triggering on any beam coming down the beam line. The active veto will trigger for any beam that is off the target location. The KATANA veto produced a signal if the beam passed through the TPC un-reacted, causing no nuclear collision; this produces a veto signal with a width of $4\mu\text{s}$ which is the approximate time it takes for the beam to drift and clear the field cage volume. The Kyoto multiplicity trigger produces a signal when the total number of tracks passing through both Kyoto arrays are greater than 4.

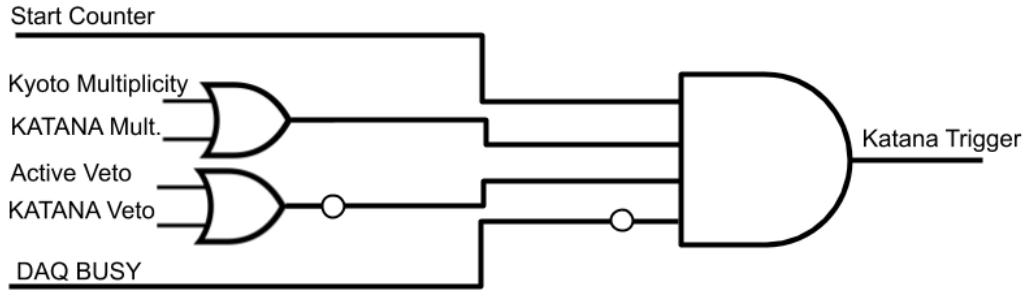


Figure 1.22: KATANA trigger box logic.

There were several special trigger considerations when we built the trigger for the TPC. We required that the gating grid be opened fast to not miss any signal; as soon as there was a condition satisfying the Start Counter, Kyoto Multiplicity, the DAQ was not busy, and there was not a KATANA Veto signal the gating-grid would be opened. This was referred to as the Fast Trigger. If the KATANA trigger box is not satisfied –described later– this will trigger a Fast Clear signal which will not trigger the DAQ, and will quickly close the gating grid. Figure 1.23 shows the logic of both of these triggers.

The master trigger for the DAQ was different for each primary beam as the experiment got

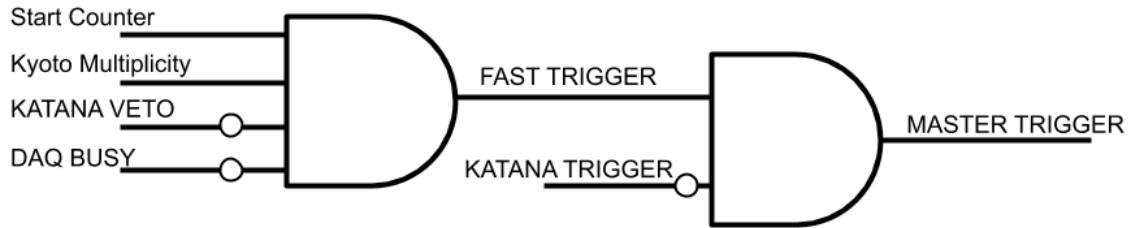
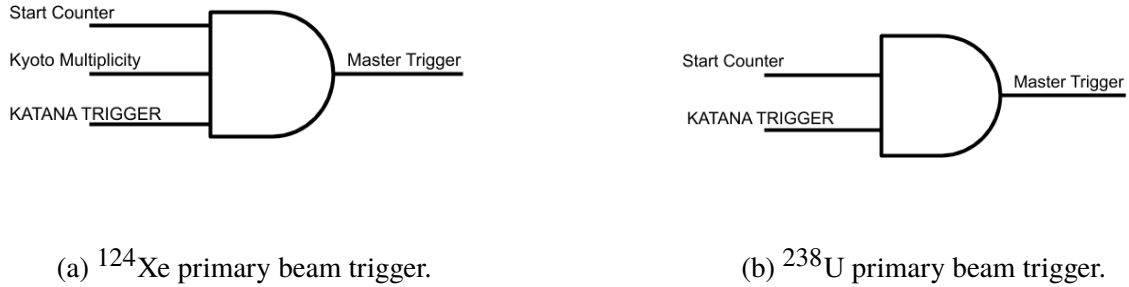


Figure 1.23: Master trigger logic.



progressively better. During the ^{124}Xe primary beam, the KATANA trigger box was an input into the trigger logic, where as in the ^{238}U primary beam, the KATANA trigger box functioned as the trigger logic utilizing the internal trigger electronics. In either case the differences in the trigger were very minor and they both behaved practically the same except for minor details on the gating-grid trigger [5]. Figure 1.22 summarizes the KATANA trigger box logic.

Figure 1.24a summarizes the ^{132}Xe primary beam, where the condition to produce a true KATANA trigger output was there must be a Start Counter, KATANA multiplicity, no Veto, and no

DAQ busy signal. The KATANA trigger, Kyoto Multiplicity, and Start Counter together triggered the DAQ.

Whereas Fig. 1.24b summarizes the ^{132}Xe primary beam, where the condition to produce a true KATANA trigger output was there must be a Start Counter, Kyoto or KATANA multiplicity, no Veto, and no DAQ busy signal. Here the KATANA trigger and the SC SUM??? together triggered the DAQ.

It is worth mentioning how the busy signals for the experiment were handled. The DAQ system itself produces a busy signal which was combined with the busy signals from either the opening or closing the gating grid. When opening the gating grid, it is assumed the full volume of the TPC will be read out, therefore a 11 μs gate busy signal is produced; which is slightly more than the time it takes for all the electrons to drift in the field cage. In the case where the gating grid should be closed, either due to the fast clear circuit or the end of the TPC measurement, a 5 μs busy signal is produced to allow for the gating grid to settle to a steady state closed configuration, and to clear the drift volume of any residual electrons from the beam. Both of these gates are included with the DAQ in an OR configuration which makes the overall busy signal.

APPENDIX

APPENDIX
RUNS ANALYZED IN THIS DATA

System	#runs	Run numbers
$^{132}\text{Sn} + ^{124}\text{Sn}$	113	2841, 2843, 2844, 2845, 2846, 2848, 2849, 2850, 2851, 2852, 2855, 2856, 2857, 2858, 2859, 2860, 2861, 2875, 2877, 2878, 2879, 2880, 2881, 2882, 2883, 2884, 2887, 2888, 2889, 2890, 2891, 2892, 2893, 2894, 2896, 2898, 2899, 2900, 2901, 2902, 2903, 2904, 2905, 2907, 2914, 2916, 2917, 2919, 2920, 2921, 2922, 2924, 2925, 2926, 2927, 2929, 2930, 2931, 2932, 2933, 2934, 2935, 2936, 2939, 2940, 2941, 2942, 2943, 2944, 2945, 2946, 2948, 2955, 2956, 2958, 2959, 2960, 2961, 2962, 2964, 2965, 2966, 2968, 2969, 2970, 2971, 2972, 2973, 2975, 2976, 2977, 2978, 2979, 2980, 2981, 2982, 2983, 2984, 2985, 2986, 2988, 2989, 2990, 2991, 2992, 2993, 2997, 2999, 3000, 3002, 3003, 3007, 3039
$^{124}\text{Sn} + ^{112}\text{Sn}$	60	2542, 2543, 2544, 2546, 2547, 2548, 2552, 2553, 2554, 2555, 2556, 2557, 2558, 2559, 2560, 2562, 2563, 2564, 2565, 2566, 2567, 2568, 2569, 2570, 2571, 2572, 2573, 2574, 2575, 2578, 2579, 2580, 2581, 2582, 2583, 2584, 2585, 2586, 2587, 2588, 2589, 2590, 2591, 2592, 2593, 2594, 2595, 2596, 2597, 2598, 2599, 2600, 2601, 2617, 2618, 2619, 2620, 2621, 2622, 2623
$^{112}\text{Sn} + ^{124}\text{Sn}$	68	3059, 3061, 3062, 3065, 3066, 3068, 3069, 3071, 3074, 3075, 3076, 3077, 3078, 3080, 3081, 3082, 3083, 3084, 3085, 3087, 3088, 3089, 3090, 3091, 3092, 3093, 3094, 3095, 3097, 3098, 3102, 3103, 3138, 3139, 3140, 3141, 3142, 3143, 3144, 3145, 3146, 3148, 3149, 3150, 3151, 3152, 3153, 3154, 3155, 3156, 3157, 3158, 3159, 3165, 3166, 3167, 3168, 3169, 3170, 3171, 3172, 3177, 3179, 3180, 3181, 3182, 3183, 3184
$^{108}\text{Sn} + ^{112}\text{Sn}$	85	2272, 2273, 2274, 2275, 2276, 2283, 2284, 2285, 2286, 2288, 2289, 2291, 2310, 2311, 2314, 2315, 2320, 2322, 2323, 2324, 2325, 2331, 2332, 2333, 2334, 2335, 2336, 2337, 2340, 2341, 2362, 2363, 2368, 2369, 2370, 2371, 2372, 2373, 2374, 2375, 2378, 2379, 2380, 2381, 2382, 2383, 2384, 2385, 2386, 2387, 2388, 2389, 2391, 2392, 2393, 2394, 2395, 2396, 2397, 2398, 2399, 2400, 2401, 2402, 2429, 2432, 2433, 2434, 2437, 2438, 2439, 2440, 2442, 2453, 2461, 2462, 2463, 2501, 2502, 2503, 2505, 2506, 2507, 2508, 2509

Table .1: List of runs for the analysis.

APPENDIX

SECOND APPENDIX

BIBLIOGRAPHY

BIBLIOGRAPHY

- [1] E. Pollacco, et al., Get: A generic electronics system from tpcs and nuclear physics instrumentation, Nuclear Instruments and Methods in Physics Research Section A:Accelerators, Spectrometers, Detectors and Associated Equipment 887 (2018) 81–93.
- [2] H. Bichsel, A method to improve tracking and particle identification in tpcs and silicon detectors, Nuclear Instruments and Methods in Physics Research Section A:Accelerators, Spectrometers, Detectors and Associated Equipment 562 (2006) 154–197.
- [3] Y. Yano, The ri beam factory project: A status report, Nucl. Instrum. Meth. B 261 (1-2) (2007) 1009–1013. doi:10.1016/j.nimb.2007.04.174.
- [4] T. Kobayashi, et al., Samurai spectrometer for ri beam experiments, Nucl. Instrum. Meth. B 317 (2013) 294–304. doi:10.1016/j.nimb.2013.05.089.
- [5] J. E. Barney, Charged pion emission from reactions with the srit time projection chamber, Ph.D. thesis (2019).
- [6] M. Capeans, Aging and materials: lessons for detectors and gas systems, Nuclear Instruments and Methods in Physics Research Section A: Accelerators, Spectrometers, Detectors and Associated Equipment 515 (1) (2003) 73 – 88. doi:<https://doi.org/10.1016/j.nima.2003.08.134>.
- [7] W. Blum, W. Riegler, L. Rolandi, Particle Detection with Drift Chambers, Springer, Berlin, Heidelberg, 2008.
- [8] E. Pollacco, et al., Get: A generic and comprehensive electronics system for nuclear physics experiments, Physics Procedia 37 (2012) 1799–1804. doi:10.1016/j.phpro.2012.02.506.
- [9] L. Landau, On the energy loss of fast particles by ionization, J. Phys. USSR 8 (201).
- [10] P. Shulek, Fluctuations of ionization loss, Sov. J. Nucl. Phys 4.
- [11] H. Bichsel, Straggling of heavy charged particles: Comparison of born hydrogenic-wavefunction approximation with free-electron approximation, Phys. Rev. B 1 (1970) 2854.
- [12] E. Gatti, et al., Optimum geometry for strip cathodes or grids in mwpc for avalanche localization along the anode wires, Nucl. Instr. Meth. Phys. Res. A 163 (1979) 83–92. doi:10.1016/0029-554X(79)90035-1.
- [13] Geodetic systems, vstars photogrammetry.
URL <https://www.geodetic.com/products/systems/v-stars-n/>